

Nematic Ordering, Conjugation, and Density of States of Soluble Polymeric Semiconductors

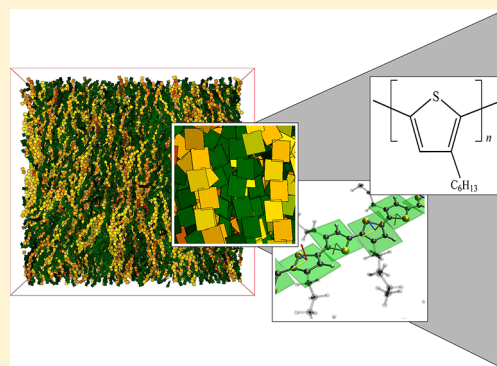
Patrick Gemünden,^{†,‡} Carl Poelking,[†] Kurt Kremer,[†] Denis Andrienko,[†] and Kostas Ch. Daoulas^{†,‡,*}

[†]Max Planck Institute for Polymer Research, 55128 Mainz, Germany

[‡]InnovationLab GmbH, 69115 Heidelberg, Germany

S Supporting Information

ABSTRACT: We develop a generic coarse-grained model for describing liquid crystalline ordering of polymeric semiconductors on mesoscopic scales, using poly(3-hexylthiophene) (P3HT) as a test system. The bonded interactions are obtained by Boltzmann-inverting the distributions of coarse-grained degrees of freedom resulting from a canonical sampling of an atomistic chain in Θ -solvent conditions. The nonbonded interactions are given by soft anisotropic potentials, representing the combined effects of anisotropic π - π interactions and entropic repulsion of side chains. We demonstrate that the model can describe uniaxial and biaxial nematic mesophases, reproduces the experimentally observed effect of molecular weight on phase behavior, and predicts Frank elastic constants typical for polymeric liquid crystals. We investigate charge transport properties of the biaxial nematic phase by analyzing the length distribution of conjugated segments and the internal energetic landscape for hole transport. Results show how conjugation defects tend to localize near chain ends and how long-range orientational correlations lead to a spatially correlated, non-Gaussian density of states.



I. INTRODUCTION

Solution-processable semiconducting polymers are considered to be potential candidates for mechanically flexible solar cells and field-effect transistors.^{1–4} A typical example is a recently certified 5.2%-efficient fully polymeric solar cell.⁵ The molecular architecture of conjugated polymers comprises a semirigid conjugated backbone, responsible for charge conductance, and flexible side chains ensuring solubility and facilitating processing (see Figure 1). Within this structural motif, the electronic and self-assembling properties of a polymer can be fine-tuned by an appropriate chemical design and selection of processing conditions. Narrowing the optical band gap, for example, has helped to improve light absorption of thin films and hence solar cell efficiency,⁶ while the use of high “boiling-temperature” solvents/additives has allowed a better control of donor/acceptor phase separation leading to improved exciton splitting and charge extraction.^{7,8}

Molecular arrangement, or morphology, of a semiconducting polymer turned out to be the most difficult to characterize, predict, or control. Most conjugated polymers are polymorphs^{9–11} and form polycrystalline, or/and partially amorphous films with hierarchical structuring of the ordered phase. Experimental reconstruction of such molecular arrangements is a formidable task. Typical diffraction patterns^{12–14} have only a few (broad) peaks, while interpreting solid-state NMR data is difficult due to the heterogeneous, on a local scale, environment.¹⁵ On the theory/simulation side the situation is not much better: atomistic molecular dynamics simulations become

impractical due to limited time- and length-scales they can address.

As an alternative, one can consider coarse-grained models with “soft” interactions^{16–18} which have a long-standing tradition in soft condensed matter physics.^{16–20} Soft models are often linked to field-theoretical descriptions^{21–30} and typically do not incorporate enough microscopic details needed for understanding electronic processes occurring in polymeric organic semiconductors. Here, we develop a soft model capable of describing large-scale (possibly nonequilibrium) liquid crystalline (LC) morphologies of conjugated polymers, while at the same time retaining enough details needed for the evaluation of material electronic properties. Specifically, each repeat unit of a polymer is mapped onto an interacting site in such way that the atomistic details can be reintroduced later, if required. The bonded potentials are chosen such that the distributions of the relevant degrees of freedom of the soft and all-atom models match. The nonbonded interactions are tuned to reflect the subtle balance between the conformational frustration of alkyl side chains and strong directional π - π interactions. They are introduced empirically, following works of Straley³¹ in liquid crystals. Namely, the conjugated π -systems of the backbone (e.g., thiophene rings) are treated as plate-like

Received: March 28, 2013

Revised: June 13, 2013

Published: July 2, 2013



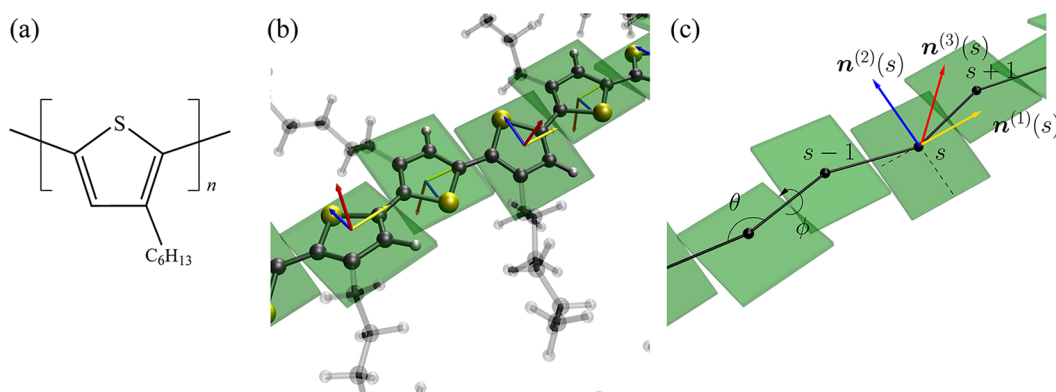


Figure 1. (a) Chemical structure of poly(3-hexylthiophene) (P3HT). (b) Atomistic and (c) coarse-grained representations of the P3HT chain. In the coarse-grained model each repeat unit is a single interacting site placed at the intersection of two imaginary lines along the bonds connecting the thiophene rings. This choice improves the transferability of the coarse-grained potential.

objects and their mutual interaction is incorporated via soft *anisotropic* potentials.

Our particular interest will be in LC mesophases,^{32–39} located between the melting temperature and the isotropic liquid state.³⁸ These mesophases are claimed to facilitate more ordered morphologies upon thermal annealing^{35,36,40} and thus improved electronic material properties, e.g., charge-carrier mobility.³⁷ As an underlying atomistic system, we have chosen poly(3-hexylthiophene) (P3HT) which belongs to a family of poly(3-alkylthiophenes), has long been a workhorse of the organic electronics community and, as such, is extensively characterized. Although observing LC mesophases in P3HT is confounded by the small gap between the melting and the thermal degradation temperatures,³⁸ several experiments have reported nematic^{32,33} or smectic-like^{35,41} ordering. In general, nematic mesophases have been reported for poly(3-alkylthiophenes) with various alkyl side groups,³⁸ and hence, the approach we employ here is extendable to a wide range of soluble polymeric semiconductors.

The paper is organized as follows. We first introduce the model and parametrize it using an all-atom representation of P3HT. Liquid crystalline mesophases of this polymer are then characterized by analyzing order parameters, elastic constants, and chain configurations. The latter are linked to the distribution of lengths of conjugated segments and intra-molecular site energy disorder (density of states) for the hole transport.

II. MODEL

The model is based on an ansatz often used in coarse-grained modeling of soft matter.⁴² Namely, the coarse-grained interactions are separated into bonded and nonbonded, and the coarse-grained degrees of freedom are assumed to be independent of each other. Each repeat unit, that is a thiophene ring with an attached hexyl side chain, is replaced by a single interaction site, as shown in Figure 1. Note that placing the interaction site at the center of mass of the thiophene ring would lead to unwanted correlations between the angular, θ , and torsional, ϕ , degrees of freedom.⁴³ These correlations can, however, be minimized by placing the site at the intersection of two imaginary lines along the bonds connecting the thiophene rings. This improves the transferability of the coarse-grained potential, i.e., temperature changes on the order of $\pm 20\%$ have negligible effect on the parameter values. The bonded interaction potentials are obtained from the conformational

sampling of a single chain, while the nonbonded interactions are captured via a phenomenological potential, as discussed below.

A. Bonded Interactions. The bond length b in the coarse-grained model is constrained to 0.4 nm. The angular and torsional interaction potentials are described by using the harmonic angular and Ryckaert-Bellemans torsion potentials, respectively:

$$V_{\theta} = \frac{\kappa_{\theta}}{2} (\theta - \theta_0)^2, \quad V_{\phi} = \sum_{j=0}^s (-1)^j c_j \cos^j \phi \quad (1)$$

To determine κ_{θ} , θ_0 , and c_j , a molecular-dynamics all-atom simulation of a P3HT 20-mer is performed at 370 K using the Langevin-dynamics algorithm as implemented in the GRO-MACS⁴⁴ package and a coupling constant $\tau = 1$ ps for the Langevin thermostat. A reparametrized version of the OPLS-AA force field is used^{45,46} with all nonbonded interactions between the thiophene rings and associated side chains further than two repeat units apart excluded during this run (in other words, we switch off all interactions beyond 1–4). The reparametrization is required since the OPLS-AA force field does not accurately model inter-ring torsional potentials in conjugated systems.⁴⁷ The force-field details can be found in the Supporting Information of ref 48.

The fit of the Boltzmann-inverted distributions P_{θ} and P_{ϕ} to eqs 1 using the VOTCA package⁴⁹ yields $\theta_0 = 147.46^\circ$, $\kappa_{\theta} = 462.653$ kJ/mol rad², $c_0 = 2.75248$, $c_1 = -1.37645$, $c_2 = -5.29397$, $c_3 = 3.19667$, $c_4 = 3.12177$, and $c_5 = -2.41059$, all in kJ/mol.

B. Nonbonded Interactions. *1. Anisotropic Interaction.* Effective nonbonded interactions in conjugated polymers are comprised of entropic (conformational frustration of side-chains) and enthalpic (π – π stacking of backbones) contributions. Incorporating these effects into coarse-grained potentials transferable across different thermodynamic states is a formidable task.^{42,50,51} Achieving transferability becomes particularly challenging for systems with heterogeneous structuring on several length scales, such as lamellar, nematic, or discotic mesophases.

In this work, the directionality of effective nonbonded interactions between thiophene units (including hexyl side groups) is mimicked by a phenomenological potential introduced after considering the coarse-grained oligomers as objects with plate-like (D_{2h} symmetry) anisotropy as is often

done in theoretical approaches to biaxial LC phases.^{31,52,53} Namely, an s -th site in a molecule i is assigned an orthonormal set of vectors $\{\mathbf{n}_i^{(1)}(s), \mathbf{n}_i^{(2)}(s), \mathbf{n}_i^{(3)}(s)\}$, where $i = 1, \dots, n$ and $s = 1, \dots, N$ (cf. Figure 1). Here n is the number of molecules in the system and N is the degree of polymerization. The orientation of these vectors is fixed by the conformation of the chain and is shown in Figure 1c: $\mathbf{n}_i^{(1)}(s)$ is parallel to $\mathbf{r}_i(s+1) - \mathbf{r}_i(s-1)$ and $\mathbf{n}_i^{(2)}(s)$ is parallel to $(\mathbf{r}_i(s+1) + \mathbf{r}_i(s-1))/2 - \mathbf{r}_i(s)$, where $\mathbf{r}_i(s)$ is the position of the interaction site s in a molecule i . The orientation of $\mathbf{n}_i^{(3)}(s)$ is given by the orthonormality of the set. For the ends of the chain the orientation vectors can be defined by adding “ghost” bonds. The torsional and angular degrees of freedom of these auxiliary bonds are also subjected to the potentials of eq 1.

The nonbonded potential between sites s and t in the i -th and j -th chain, respectively, has the following form:^{31,52–54}

$$V_{\text{nb}} = u(r_{ij}(s, t)) \left[\bar{\kappa} - \frac{2\bar{\nu}}{3} q_i^{(1)}(s) : q_j^{(1)}(t) - \frac{2\bar{\mu}}{3} (q_i^{(1)}(s) : b_j(t) + b_i(s) : q_j^{(1)}(t)) - \frac{\bar{\lambda}}{2} b_i(s) : b_j(t) \right] \quad (2)$$

where $r_{ij}(s, t) = |\mathbf{r}_i(s) - \mathbf{r}_j(t)|$. The isotropic part of the interaction is set by $u(r_{ij}(s, t))$ and $\bar{\kappa}$ controls the compressibility of the system. The molecular tensors $\mathbf{q}^{(k)}$ (where $k = 1, 2, 3$) and \mathbf{b} are defined as:

$$q_{i,\alpha\beta}^{(k)}(s) = \frac{3}{2} n_{i,\alpha}^{(k)}(s) n_{i,\beta}^{(k)}(s) - \frac{\delta_{\alpha\beta}}{2} \quad (3)$$

$$b_{i,\alpha\beta}(s) = n_{i,\alpha}^{(2)}(s) n_{i,\beta}^{(2)}(s) - n_{i,\alpha}^{(3)}(s) n_{i,\beta}^{(3)}(s) \quad (4)$$

where $\alpha, \beta = x, y, z$. Within the above definition of molecular tensors, the $\bar{\nu}$ -dependent term in eq 2, corresponding to the scalar inner product⁵⁵ of $\mathbf{q}_i^{(1)}(s)$ and $\mathbf{q}_j^{(1)}(t)$, promotes a “rod-like” nematic alignment, where (on average) $\mathbf{n}_i^{(1)}(s) \parallel \mathbf{n}_j^{(1)}(t)$. The term defined by the product of $\mathbf{b}_i(s)$ and $\mathbf{b}_j(t)$ facilitates biaxial ordering, where (on average) $\mathbf{n}_i^{(2)}(s) \parallel \mathbf{n}_j^{(2)}(t)$ and $\mathbf{n}_i^{(3)}(s) \parallel \mathbf{n}_j^{(3)}(t)$. Finally, the $\bar{\mu}$ -dependent term favors an (on average) orthogonal orientation of hexylthiophene units, i.e., where $\mathbf{n}_i^{(1)}(s) \perp \mathbf{n}_j^{(1)}(t)$ and $\mathbf{n}_i^{(2)}(s) \perp \mathbf{n}_j^{(2)}(t)$. In this work, such orientation of mesogens will be considered unphysical and in the following we set everywhere $\bar{\mu} = 0$. Note that if sites s and t are located on the same chain and $|s - t| \leq 3$, their nonbonded interactions are set to zero, otherwise they interact with the potential defined in eq 2.

The presence of the distance-dependent soft core $u(r_{ij}(s, t))$ makes the interaction potential, eq 2, different from the one introduced by Straley.³¹ In that work the potential was obtained from the excluded volume of two rectangular blocks at selected relative orientations and the distance-dependence was averaged out as the first step for the mean field treatment. The directional interactions of eq 2 can be considered as a simple case of defining a coarse-grained potential by keeping a few terms in a general representation through an expansion into a product basis of Wigner matrices.^{56,57} Generally, the coefficients in such an expansion are functions of intermolecular distances. Our model approximates these dependencies by a single function, $u(r_{ij}(s, t))$, which is defined in the next section.

2. Soft Repulsive Core Interaction. Factorization of the nonbonded interactions into the distance- and orientation-

dependent parts, as it has been done in eq 2, is typical for LC models with soft anisotropic cores.^{58–63} For the distance-dependent part, $u(r_{ij}(s, t))$, various forms have been proposed, from quadratic polynomials⁶⁴ to more elaborated functions.⁶⁵

Here we use a soft repulsion potential obtained³⁰ from the overlap of two spherical, constant, density distributions, $\omega(\mathbf{r})$, placed at $\mathbf{r}_i(s)$ and $\mathbf{r}_j(t)$:

$$u(r_{ij}(s, t)) = \frac{1}{\rho_0} \int d\mathbf{r} \omega(\mathbf{r} - \mathbf{r}_i(s)) \omega(\mathbf{r} - \mathbf{r}_j(t)) \\ = \frac{3}{8\pi\rho_0\sigma^3} \left(2 + \frac{r_{ij}(s, t)}{2\sigma} \right) \left(1 - \frac{r_{ij}(s, t)}{2\sigma} \right)^2 \quad (5)$$

The normalized density distribution is set to $\omega(\mathbf{r}) = 3/(4\pi\sigma^3)$ when $r \leq \sigma$, and is zero otherwise.

In order to fix the sphere diameter, $d = 2\sigma$, which determines the interaction range, we note that conjugated backbones start to repel each other when their side chains overlap. We therefore set $\sigma = 0.6$ nm which is close to the length of a hexyl chain in the all-trans configuration, ~ 0.76 nm.

Note that we retain the explicit dependence of the potential $u(r_{ij}(s, t))$ on a reference density ρ_0 , although it could have been incorporated into the coefficients of eq 2. As shown in the Supporting Information, this emphasizes a link to an alternative definition of interactions through collective degrees of freedom used in field-theoretical descriptions of polymeric liquid crystals.^{66–69} For simulations, the reference density is chosen to be the bulk number density of P3HT repeat units, ~ 4 hexylthiophenes/nm³, which is estimated from the P3HT molar volume of 151 cm³/mol.⁷⁰

3. Setting the Interaction Strength. Obtaining physically adequate thermodynamic behavior of the system imposes constraints on $\bar{\kappa}$, $\bar{\nu}$, $\bar{\mu}$, and $\bar{\lambda}$. As has been already mentioned above, we always set $\bar{\mu} = 0$ and consider in the $\bar{\nu}$, $\bar{\lambda}$ -parameter space two limiting cases. Namely, when $\bar{\nu} = 0$ and $\bar{\lambda}$ is larger than a critical value, we obtain biaxial nematic mesophases. When exploring the properties of such mesophases related to charge transport (e.g., density of states) it is important to ensure that the same parametrization leads to biaxial nematic ordering for all considered molecular weights and temperatures. For this purpose, we take into account that the magnitude of $\bar{\lambda}$ required to induce biaxial ordering decreases when increasing the chain length (see section IV.B for details). Therefore, we explore initially the LC behavior of the shortest polymer, $N = 8$, at the highest temperature of interest, $T_0 = 500$ K, and choose for $\bar{\lambda}$ a value on the order of a few $k_B T_0$, for which biaxial nematic ordering is observed. This choice of $\bar{\lambda}$ is sufficient to induce biaxial nematic ordering for the remaining combinations of chain lengths and temperatures considered in the current simulations. We also address the opposite case setting $\bar{\lambda} = 0$, where for sufficiently large $\bar{\nu}$ mesophases with “rod-like” nematic alignment are obtained.

The restrictions on $\bar{\kappa}$ can be anticipated from the simple mean field estimation of the isothermal compressibility, κ_T , (see Supporting Information) in the case of perfect biaxial ordering:

$$\frac{1}{\kappa_T} = \frac{k_B T_0}{N} + (\bar{\kappa} - \bar{\nu} - \bar{\lambda}) \rho_0 \quad (6)$$

Within the range of coupling parameters considered in our simulations we employ $\bar{\kappa} = 6k_B T_0$ to ensure a positive compressibility.²⁷ At the same time for this choice $\bar{\kappa} u(0) =$

$6\bar{\kappa}/8\pi\rho_0\sigma^3 \approx 1.65k_B T_0$, that is, the interactions remain soft (i.e., on the scale of $k_B T$) even at strong overlaps. The latter results from the substantial degree of coarse-graining employed in the current model, while preserving the number density of hexylthiophene units of the real material. Indeed, in our case the coarse-grained hexylthiophenes interact already at distances $2\sigma = 1.2$ nm which is almost two times larger than the average distance of their centers estimated from the mean density as $\rho_0^{-1/3} \approx 0.63$ nm. In this scope, using $\bar{\kappa}$'s with higher order of magnitude would result into a model with unrealistically large excluded volumes. A more general discussion of the effects of compressibility on packing of largely coarse-grained units can be found in ref 28.

III. SIMULATION DETAILS

In the following, we consider P3HT molecules with polymerization degree $N = 8, 16$, and 32 , placed in a cubic simulation cell with fixed volume, V , and temperature, T . The number of chains in the box, n , is defined so that the average density of particles corresponds to the reference density of the P3HT, i.e., $nN/V \approx 4$ hexylthiophenes/nm³. The configuration space of these systems is sampled using a Monte Carlo approach. The scheme is based on the standard “slithering snake” (i.e., reptation) algorithm,^{71–74} adopted in our case to take into account the orientational degrees of freedom of the end-groups of the P3HT chain.

To propose a new configuration a chain is randomly selected, one of the two end-groups together with the attached “ghost” bond is cut and reattached to the opposite end of the molecule (the choice of the direction of the reptation is random, as well). The reattachment is performed through the “ghost” bond at the corresponding end of the chain (cf., section II.B), which transforms into a physical bond. Subsequently, to specify the orientation of the hexylthiophene at the changed position, new torsional and angular degrees of freedom are chosen for the “ghost” bond, which is attached to it. These are drawn according to the Boltzmann weight of the bonded potentials, defined in eqs 1. Simultaneously, at the old position of the group, the physical bond which was connecting it to the chain backbone, becomes a “ghost” bond. The above steps are clarified in Figure 2, showing a P3HT chain before and after a reptation move. Following the standard Metropolis criterion the move is accepted with probability $p_{acc} = \min(1, \exp(-\Delta E_{nb}/k_B T))$, where ΔE_{nb} corresponds to the difference in nonbonded

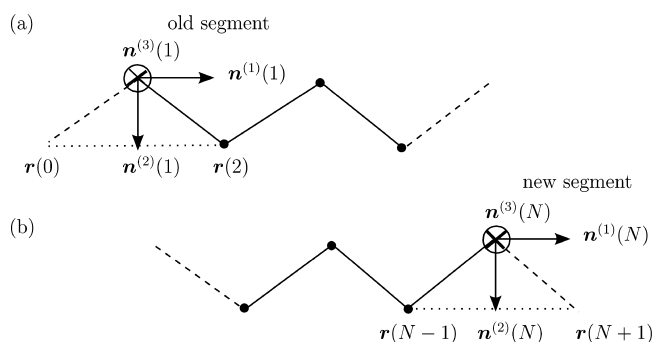


Figure 2. Configuration of a P3HT chain prior (a) and after (b) a reptation move. The physical and the “ghost” bonds are drawn with solid and dashed lines, respectively. The orthonormal set of vectors defining the orientation of the hexylthiophene group at the old and the new position is also shown.

energies between the proposed and the old configuration. It is calculated by considering the isotropic and directional interactions (see eq 2) between the displaced group and the surrounding particles at the new and old positions, using a standard neighbor-list algorithm. The softness of the interactions enhances significantly the efficiency of the reptation move, e.g., in the biaxial phase the move has an acceptance rate near 20%.

Periodic boundary conditions are employed in all directions. To reduce finite system-size effects the length of the box edges, L , is taken to be at least twice as large as the contour length of the polymer. For example, setting $L \approx 26$ nm constitutes a typical choice for the shorter P3HT chains ($N = 8$ and 16). In this case the modeled systems contain about 7×10^4 coarse-grained hexylthiophene groups. At the same time, the simulations of the longer molecules ($N = 32$) are more demanding: typical systems considered in this case have dimensions $L \approx 51$ nm and consist of approximately 5×10^5 hexylthiophenes.

IV. CONFORMATIONAL, THERMODYNAMIC, AND ELASTIC PROPERTIES

A. Amorphous Melts. Before addressing systems with orientation-dependent interactions it is instructive to model P3HT melts employing only the isotropic repulsive part of the potential in eq 2 with $\bar{\kappa} = 6k_B T_0$, while $\bar{\nu} = \bar{\mu} = \bar{\lambda} = 0$. Conformational properties of the P3HT chains can be quantified via the standard single chain structure factor, $S_0(q)$, which in the form of a Holtzer plot⁷⁵ can be related to chain stiffness. An example is shown in Figure 3a demonstrating the $qS_0(q)$ calculated in a melt of P3HT chains with $N = 32$ simulated at $T = 500$ K. The wave vector q^* marking the

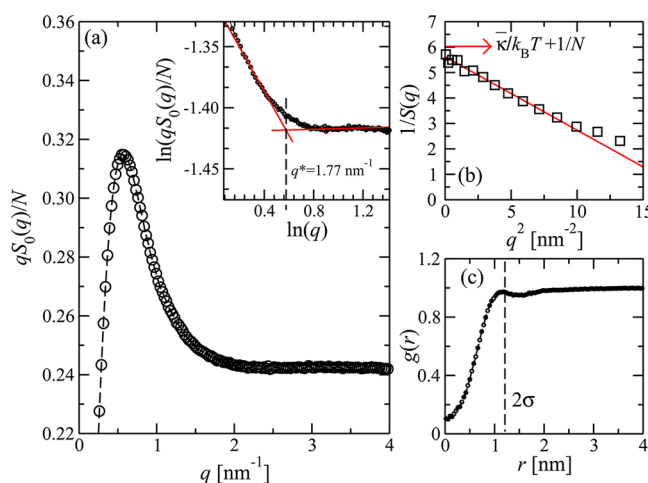


Figure 3. (a) Holtzer plot for a melt of P3HT chains with $N = 32$ where $S_0(q)$ stands for the single chain structure factor and q is the magnitude of the wave vector. The inset shows the region of the transition to the Holtzer plateau in a logarithmic plot and straight lines correspond to a linear fit of data. (b) Inverse structure factor of density fluctuations, $1/S(q)$, plotted for small wave vectors, calculated from simulations of P3HT melts with $N = 32$. For comparison the limit $1/S(q \rightarrow 0) = (\bar{\kappa}/k_B T) + 1/N$ obtained using the mean field estimation for the isothermal compressibility is marked by the arrow. (c) Pair correlation function, $g(r)$, calculated in the same system. All results shown in the figure have been obtained from simulations performed at $T = T_0 = 500$ K, setting the orientation coupling parameters to zero and $\bar{\kappa} = 6k_B T_0$.

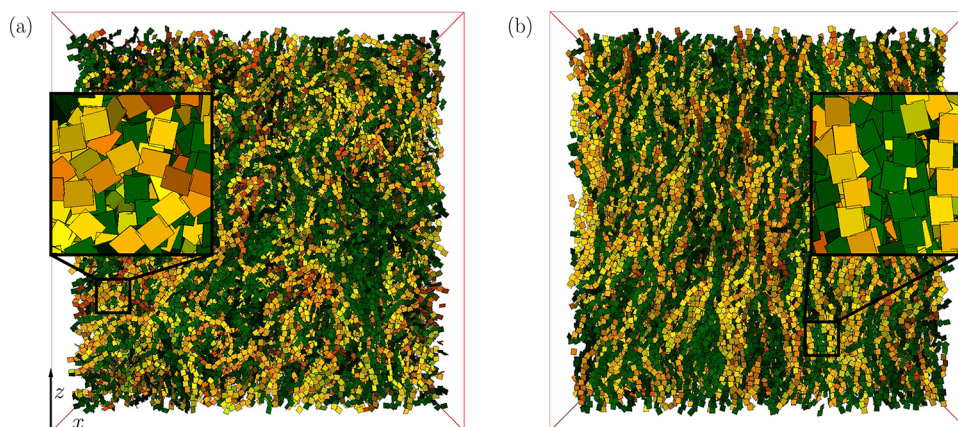


Figure 4. Both panels show a snapshot of an equilibrated system containing 2169 molecules with polymerization degree $N = 32$, obtained from simulations started from a prestacked configuration. To facilitate visualization, a configuration of a relatively small system with $L \simeq 28$ nm is presented. Colors are arbitrarily chosen to improve visibility of different chains. Panel (a) demonstrates a system in a plate-like nematic phase where the coupling strength is set to $\bar{\lambda} = 4k_B T_0$. Panel (b) corresponds to a biaxial nematic system obtained at a stronger coupling $\bar{\lambda} = 5.5k_B T_0$. The thiophenes have their $\mathbf{n}_i^{(1)}(s)$, $\mathbf{n}_i^{(2)}(s)$, and $\mathbf{n}_i^{(3)}(s)$ vectors aligned (on average) along the z , x , and y -directions, respectively. In both cases, $\bar{v} = \bar{\mu} = 0$ and $T = T_0 = 500$ K.

transition to the “Holtzer plateau” can be used^{75–77} to define a persistence length $l_p = 3.5/q^*$. We choose to obtain q^* from the intersection of two straight lines by fitting in a logarithmic plot (see inset in Figure 3a) the decreasing part of $qS_0(q)$ before the plateau, i.e., within the interval $1.21 \text{ nm}^{-1} \leq q \leq 1.58 \text{ nm}^{-1}$, and the plateau regime itself, i.e., $2.41 \text{ nm}^{-1} \leq q \leq 3.46 \text{ nm}^{-1}$. From Figure 3a, we find $q^* = 1.77 \text{ nm}^{-1}$ leading to $l_p = 1.98$ nm. As has been discussed in ref 77, the choice of the fitting region and of the function approximating the $qS_0(q)$ near the plateau is rather ambiguous and such details will affect the precise values of the extracted l_p . Thus, when comparing simulation results with scattering experiments it is essential that both employ the same definition of l_p and conventions for its extraction. However, it is noted that the $l_p = 1.98$ nm calculated from the Holtzer plateau is comparable to $l_p = 1.5 \text{ nm} - 2 \text{ nm}$ observed in scattering experiments⁷⁸ for P3HT solutions near Θ -solvent conditions at high temperatures ($T \sim 200$ °C). In this case, rather long P3HT chains were considered which facilitated extracting an l_p by fitting the $S_0(q)$ with the approximate analytical form of Sharp and Bloomfield.^{79,80}

The compressibility of the amorphous melt can be estimated from the structure factor of the density correlation function defined as:

$$S(q) = \frac{1}{nN} \langle |\sum_{i,s}^{n,N} \exp(i\mathbf{q} \cdot \mathbf{r}_i(s))|^2 \rangle \quad (7)$$

where the brackets denote an average over the directions of the wave vector \mathbf{q} and the configurations of the system. The isothermal compressibility is obtained⁸¹ as $\rho_0 k_B T k_T = S(q \rightarrow 0)$. In Figure 3b we demonstrate the behavior of $1/S(q)$ as a function of q^2 for small wave vectors and it can be seen that the $1/S(q)$ has a characteristic Ornstein–Zernike (i.e., linear) dependence on q^2 . The linear dependence is highlighted by fitting the data with $q^2 \lesssim 10 \text{ nm}^{-2}$ to a straight line. Interestingly the compressibility is rather close to the (approximate) mean field prediction $1/\rho_0 k_B T k_T = (\bar{\kappa}/k_B T) + 1/N$ (cf., eq 6) although the experimental densities realized in our simulations are low comparing to the “infinitely high” density limit assumed in the former. This is illustrated in Figure 3c by the radial distribution function, $g(r)$, exhibiting a distinct

structuring which contrasts²⁰ $g(r) = 1$ of the mean field limit. Atomistic simulations of P3HT melts at high temperatures estimate⁸² the region of “hard” excluded volume between hexylthiophene groups to be $r \approx 0.5$ nm. Although the excluded volume constraint is relaxed in our case, it can be seen that after the first coordination shell set by the size of the isotropic core, 2σ , the $g(r)$ drops substantially and $g(r = 0.5 \text{ nm}) \approx 0.3$. The latter point may be important in the future, for reintroducing the atomistic details into the configurations obtained with the soft model.

B. Isotropic/Biaxial Nematic Transition. Uniaxial or biaxial nematic ordering in a configuration of a P3HT system can be identified through a combined consideration of two order parameters, S and B . Following a standard procedure,^{83,84} they can be obtained by calculating the orientation tensors $\mathbf{Q}^{(k)}$ (where $k = 1, 2, 3$) defined as

$$\mathbf{Q}_{\alpha\beta}^{(k)} = \frac{1}{nN} \sum_{i,s}^{n,N} q_{i,\alpha\beta}^{(k)}(s) \quad (8)$$

where the molecular tensors $\mathbf{q}_i^{(k)}(s)$ have been introduced in eq 3. Subsequently, a set of nine eigenvalues (three for each tensor) is determined and the eigenvalue λ_{\max} with the maximum absolute value is identified. The order parameter S can be obtained from:

$$S = |\mathbf{v}_{\max}^T \mathbf{Q}^{\max} \mathbf{v}_{\max}| \quad (9)$$

In the above, \mathbf{Q}^{\max} and \mathbf{v}_{\max} (with $|\mathbf{v}_{\max}| = 1$) stand for the orientation tensor and the eigenvector corresponding to λ_{\max} . Isotropic phases are characterized by a vanishing S (within corrections for finite number of particles⁸⁵) while $S > 0$ indicates nematic orientation parallel to \mathbf{v}_{\max} . In our case two types of uniaxial nematic ordering are observed: (a) rod-like, where (on average) $\mathbf{n}_i^{(1)}(s) \parallel \mathbf{v}_{\max}$ and (b) plate-like, where (on average) $\mathbf{n}_i^{(3)}(s) \parallel \mathbf{v}_{\max}$. A representative snapshot of a plate-like nematic mesophase is shown in Figure 4a. A straightforward way to distinguish between the two uniaxial mesophases is to monitor the sign of the maximum absolute eigenvalue of $\mathbf{Q}^{(1)}$, which will be positive in the first and negative in the second case.

To establish whether the system shows additional order perpendicular to \mathbf{v}_{\max} we choose from the six eigenvalues of the remaining two orientation tensors the one with the maximum positive value $\lambda_{2,\max}$. The orientation tensor and the eigenvector associated with this eigenvalue will be denoted as $\mathbf{Q}^{2\text{nd}}$ and $\mathbf{v}_{2,\max}$, respectively. After projecting⁸⁴ $\mathbf{v}_{2,\max}$ to the plane perpendicular to \mathbf{v}_{\max} , one completes the resulting set of directors \mathbf{v}_{\max} , $\mathbf{v}_{2,\max}^{\text{pr}}$ to a right-handed orthonormal system with $\mathbf{v}_{3,\max}^{\text{pr}}$. With the help of the remaining orientation tensor, $\mathbf{Q}^{3\text{rd}}$, the order parameter B is calculated as:

$$B = \frac{1}{3} |\mathbf{v}_{2,\max}^{\text{pr},T} \mathbf{Q}^{2\text{nd},\text{pr}} \mathbf{v}_{2,\max}^{\text{pr}} + \mathbf{v}_{3,\max}^{\text{pr},T} \mathbf{Q}^{3\text{rd},\text{pr}} \mathbf{v}_{3,\max}^{\text{pr}} - \mathbf{v}_{2,\max}^{\text{pr},T} \mathbf{Q}^{3\text{rd},\text{pr}} \mathbf{v}_{2,\max}^{\text{pr}} - \mathbf{v}_{3,\max}^{\text{pr},T} \mathbf{Q}^{2\text{nd},\text{pr}} \mathbf{v}_{3,\max}^{\text{pr}}| \quad (10)$$

B constitutes a true measure of biaxial order: it grows only when two independent axes of mesogenes are ordered along the corresponding directors and vanishes in purely uniaxial phases. A representative snapshot of a biaxial nematic mesophase is shown in Figure 4b.

Following the above approach we explored for $T = T_0$ the phase behavior as a function of chain length and orientation coupling $\bar{\lambda}$, while keeping, as explained in section II.B, $\bar{\nu} = \bar{\mu} = 0$. Our findings are summarized in Figure 5a, showing the

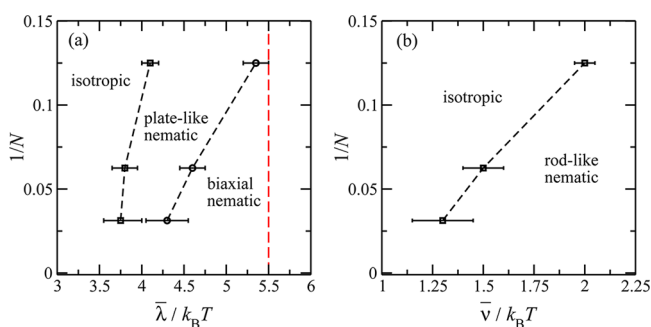


Figure 5. (a) Phase behavior as a function of inverse degree of polymerization, $1/N$, and orientation-coupling strength $\bar{\lambda}$ (in units of $k_B T$), for $\bar{\nu} = \bar{\mu} = 0$. The dashed red line marks the value $\bar{\lambda} = 5.5 k_B T_0$ used to obtain morphologies with biaxial structuring for charge transport calculations. (b) Phase behavior as a function of inverse degree of polymerization, $1/N$, and orientation-coupling strength $\bar{\nu}$ (in units of $k_B T$) for $\bar{\lambda} = \bar{\mu} = 0$. In both cases the highest temperature, $T = T_0 = 500$ K, was considered.

approximate (details follow below) location of the different phases as a function of $\bar{\lambda}$ and inverse polymerization degree, $1/N$. It can be seen that for all N 's considered here, the onset of biaxial ordering as a function of $\bar{\lambda}$ occurs in two steps. First for moderate coupling strengths one observes a crossing from an isotropic system into a plate-like nematic mesophase, characterized by $S \approx 0.5$ – 0.8 . Although in the plate-like nematic mesophase the biaxial order parameter B increases slightly comparing to isotropic systems it remains small, i.e., $B \leq 0.1$. By increasing further $\bar{\lambda}$ we obtain mesophases with biaxial structuring, characterized by $B \approx 0.3$ – 0.6 . Notably for the systems considered in our study B is always lower than S and usually shows larger fluctuations. For each N the boundaries between the phases were located by observing spontaneous ordering of the system from a random initial configuration. In this scope, the error bars represent the regimes close to the transition, where strong fluctuations of S and B did not allow for a definite conclusion regarding the state

of the system. For the longest chains, $N = 32$, (where one expects the most significant finite-size effects) the boundaries of the phases were estimated for two different box sizes ($L = 64 b$ and $L = 128 b$) yielding, within the accuracy of the current study, the same results. Figure 5a highlights that indeed for longer chains the biaxial nematic ordering takes place at weaker orientation couplings as has been already mentioned in section II.B. Similar effects of molecular weight on the onset of LC ordering are observed in the case of uniaxial rod-like mesophases. As an illustration, Figure 5b demonstrates the phase behavior obtained at $T = T_0$, as a function of chain length and orientation coupling $\bar{\nu}$, while keeping $\bar{\mu} = \bar{\lambda} = 0$. This result agrees with earlier simulations of rod-like nematic phases of poly(3-alkylthiophenes) based on a simpler model²⁷ and experimental observations.³⁸ The latter report that increasing the molecular weight of the polymer shifts the isotropic/nematic transition to higher temperatures, i.e., (in terms of our study) for longer chains, weaker thermodynamic orientational forces ($\sim \bar{\nu}/k_B T$) are required to obtain nematic LC ordering.

C. Estimating Elastic Properties in the Nematic Phase.

Spatial inhomogeneities in the orientation of mesogenes can be considered within continuum Frank-type free-energy descriptions, associating the thermodynamic penalty of changes in the orientation of the director(s) with a set of certain elastic constants. Despite the softness of our model, which results in a higher compressibility (i.e., lower bulk modulus, E) of coarse-grained P3HT compared to the real material, it will be demonstrated here that it reproduces a reasonable order of magnitude for the Frank elastic constants.

We will focus on the simple case of nonbiaxial nematic mesophases, where the variations in the orientation of the director are penalized by the splay, K_1 , twist, K_2 , and bending, K_3 , elastic constants.⁸⁶ In this scope, melts of P3HT chains with $N = 32$ were considered, at $T = T_0$, setting $\bar{\mu} = \bar{\lambda} = 0$ while employing three different strengths for the nematic orientation-coupling parameters $\bar{\nu} = 1.8 k_B T_0$, $2 k_B T_0$, and $2.5 k_B T_0$. Two different box-sizes $L = 64 b$ and $128 b$ (corresponding to roughly two and four times the end-to-end distance of a fully stretched P3HT molecule, respectively) were considered to ensure that there were no significant finite system-size effects. The MC simulations were started from a perfect biaxial nematic mesophase with all P3HT chains in a trans configuration and all thiophene units having their $\mathbf{n}_i^{(1)}(s)$ and $\mathbf{n}_i^{(3)}(s)$ vectors aligned along the z - and the y -axis of the box, respectively. After relaxation, a rod-like nematic mesophase was obtained.

Following a standard approach in liquid crystals^{86–88} we analyze a large number of equilibrated configurations calculating for each of them the Fourier transform of the local nematic tensor as:

$$\hat{Q}_{\alpha\beta}^{(1)}(\mathbf{q}) = \frac{1}{\rho_0} \sum_{i=1}^n \sum_{s=1}^N q_{i,\alpha\beta}^{(1)}(s) \exp(i\mathbf{q} \cdot \mathbf{r}_i(s)) \quad (11)$$

In systems of nematic liquid crystals with small mesogenes, relating the fluctuations in the orientation of the local director to the Frank elastic constants through the tensor $\hat{Q}^{(1)}(\mathbf{q})$ is straightforward.^{87,88} However, the case of nematic polymer melts becomes more complex. Since polymer chains are mesoscopic objects, splay deformations are coupled to local changes of density.⁸⁹ Because of the low compressibility of polymer melts, this yields K_1 that are significantly higher than K_2 and K_3 . Additional mechanisms commensurate with splay deformations under a constant density include hairpin

formation⁸⁹ and insertion of chain ends,⁹⁰ also yielding high K_1 values.

The first theoretical description of the elastic constants in melts of compressible polymer nematics was developed by de Gennes.⁸⁹ Within this theoretical framework, for the orientation of the mesophase in our simulations where the macroscopic nematic director is aligned along the z -axis of the laboratory frame (we verify that the macroscopic director does not rotate during the simulation) the following relationships hold:

$$K_2 q_y^2 + K_3 q_z^2 = \frac{9k_B T V \langle S \rangle^2}{4 \langle |\hat{Q}_{xz}^{(1)}(\mathbf{q})|^2 \rangle} \quad (12)$$

$$K_1 q_y^2 + K_3 q_z^2 = \frac{9k_B T V \langle S \rangle^2}{4 \langle |\hat{Q}_{yz}^{(1)}(\mathbf{q})|^2 \rangle} \quad (13)$$

where for the wave vector we use $\mathbf{q} = \{0, q_y, q_z\}$, while angular brackets denote a thermal average. Formally, these relationships are similar to those in the case of small mesogenes, however, in the current case K_1 presents an effective elastic constant with contributions from a "genuine" Frank elastic free-energy and the equation-of-state of the material. In general, K_1 will be a function of q . The theory of de Gennes predicts two regimes⁸⁹ depending on how the length-scale of the scattering compares with the contour length of the chain, L_c . For $q_z L_c / 2\pi \ll 1$, it should be $K_1 = EL_c^2 / 12$, while for $q_z L_c / 2\pi \gg 1$, the limit of infinite chains is applicable, where $K_1 = K'_1 + E/q_z^2$. We note that for the first regime the chain-end-insertion mechanism of Meyer^{86,90} yields a different scaling, $K_1 \sim L_c$.

In the simulations the set of the scattering vectors is determined by the box size, i.e., $q_\alpha = 2\pi m_\alpha / L$ where m_α are integers. Because of the length of the P3HT chains modeled here (i.e., $N = 32$) there are no mesoscopic length-scales between the contour-length, $L_c \approx Nb$, and the microscopic length of the bond, b , where a continuum description could be applied. Thus, the high- q limit can not be addressed here and we focus on the regime $-4 \leq m_\alpha \leq 4$ where K_1 is affected by the finite length of the chains. We estimate the elastic constants by performing a two-dimensional fit in the reciprocal space of the right-hand sides of eqs 12 and 13 with a polynomial basis $\{1, q_y^2, q_z^2\}$. For both equations the fits of the simulation data are of good quality. For the case of the coupling strength $\bar{\nu} = 2.5k_B T_0$ this analysis yields $K_2 = 0.8 \times 10^{-11}$ N and $K_3 = 2.2 \times 10^{-11}$ N. For the splay constant we obtain $K_1 = 5.2 \times 10^{-11}$ N. For eq 13 the best fit is obtained by assuming that K_1 is independent of q_z in the small wave vector regime, as suggested by the theory of de Gennes. We note that the elastic constants remain on the order of 10^{-11} N also for the other strengths of nematic coupling mentioned above, that is, for $\bar{\nu} = 1.8k_B T_0$ and $2k_B T_0$.

In low molecular weight liquid crystals the twist and bending elastic constants are typically on the order of 10^{-12} N.⁸⁸ Experimental measurements in thermotropic main-chain polymer nematics have reported K_2 and K_3 that are either comparable^{91,92} or two orders of magnitude⁹³ larger. In our soft model the K_2 and K_3 are on the order of 10^{-11} N which fits well into the window of values reported experimentally. The relative magnitude of the two constants observed in the simulations, that is $K_3 > K_2$, agrees also with experimental trends.⁹²

Experiments demonstrate that the splay constant should be one^{91,92} or two⁹³ orders of magnitude larger than the twist and

bending constants. For the rather short chains considered in our simulations, the K_1 is substantially larger than K_2 and K_3 although it is still of the order of 10^{-11} N. We expect that in simulations with chains of higher molecular weight the splay constant will significantly increase. To support this statement, the three elastic constants were calculated for systems with $N = 8$ and $N = 16$ ($\bar{\nu} = 2.5k_B T_0$) using the same method. The K_1 , K_2 , and K_3 as a function of polymerization degree are presented in Figure 6, demonstrating that indeed K_1 increases monotonically

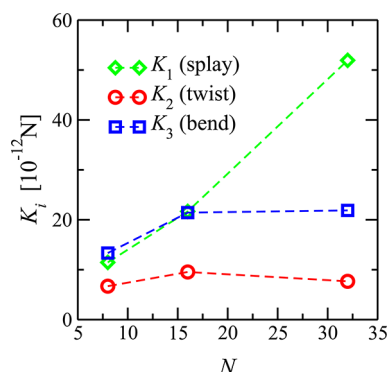


Figure 6. Dependence of the three Frank elastic constants on the degree of polymerization, N , in a uniaxial rod-like nematic mesophase. The coupling strength was set to $\bar{\nu} = 2.5k_B T_0$ and the temperature to $T = T_0 = 500$ K.

with N as predicted by both the de Gennes and Meyer mechanisms. Modeling longer chains, however, is necessary to determine the form of the functional dependence. At the same time, for $N = 32$, the twist and bending constants remain small.

V. MORPHOLOGY AND PROPERTIES RELATED TO CHARGE TRANSPORT

In this section, we will link molecular conformations and cooperative chain alignment to properties relevant to charge transport. Charge transport in P3HT has been studied with the aim of relating polymer regioregularity and molecular weight to the morphology, hole mobility, and thus efficiency of bulk heterojunction solar cells. Both hole and electron time-of-flight mobilities were reported to be independent of the molecular weight up to 20 kDa, which then decreased by an order of magnitude as molecular weight was further increased to 120 kDa.⁹⁴ The field-effect mobility was found to increase with the molecular weight in spite of reduced crystallinity. This was attributed to either better interconnectivity of the polymer network⁹⁵ or smaller intrachain ring torsions present in high molecular weight molecules.⁹⁶ Computational studies of P3HT date back to the development of force-fields⁹⁷ and coarse-grained models.^{82,98} An effect of polymer chain conformation on charge localization, the density of states, and charge mobility has been studied in crystalline P3HT of different regioregularity,⁹⁹ where it was found that a trap state exists every 10–30 repeat units. A Boltzmann-weighted hopping model included the effect of polycrystallinity,¹⁰⁰ allowing to interpret anisotropic mobilities in P3HT films obtained via directional crystallization.

In partially ordered organic semiconductors charges are typically localized on molecules or their *conjugated segments*. Within these segments, π -conjugation leads to an instantaneous delocalization of a charge carrier, while between the segments π -conjugation is broken. Charge transport proceeds via a series

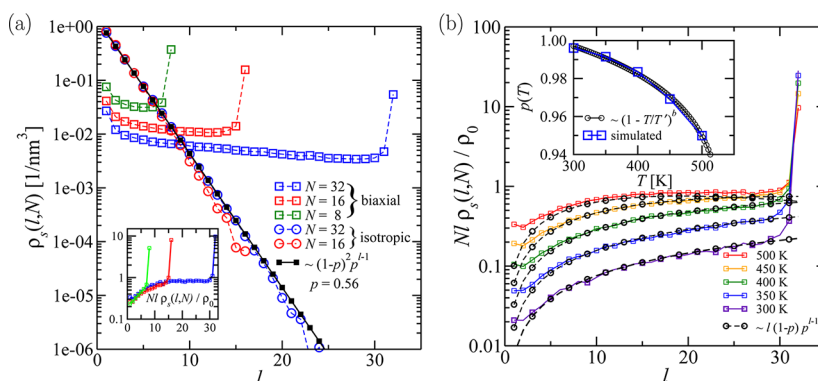


Figure 7. (a) Volume number density $\rho_s(l, N)$ of conjugated segments of length l for systems with $N = 8, 16$, and 32 thiophene units per polymer chain and fit to eq 14 in the limit $l \ll N$. Inset: Volume density ratio of monomers belonging to a conjugated segment of length l divided by the density of chains in the system, ρ_0/N . The data were obtained setting $\bar{\lambda} = 5.5k_B T_0$ and $T = T_0 = 500$ K. (b) Temperature dependence of the partial density of monomers in the range from 300 to 500 K, where $N = 32$ and $\bar{\lambda} = 5k_B T_0$. The defect density has been fit to eq 14 in the limit of $p \rightarrow 1$ via the bond conjugation probability p . The inset summarizes the dependence of p on temperature. We stress that for $N = 16$, p , as well as its temperature dependence, is identical to the case of $N = 32$.

of hopping events, that is, charge transfer reactions, between the conjugated segments. Because of spatial heterogeneity on a microscopic scale, the free energy of the system in the product and adduct states of a single transfer reaction can be different, leading to a spatially inhomogeneous, or rugged, energetic landscape and a broadened density of states (DOS). As the hopping rate depends exponentially on the product/adduct free-energy difference, charge mobility is very sensitive to the distribution of site energies, their spatial correlation, and the particular pathway a charge undertakes in a material.^{101–103}

In small-molecule-based amorphous organic semiconductors, where the charge normally delocalizes over an entire molecule, electrostatic effects (e.g., charge interacting with randomly oriented molecular dipoles) lead to a Gaussian shape of the DOS, while induction effects can lead to a non-Gaussian distribution of site energies.¹⁰⁴ Because of the long-range nature of electrostatic interactions, site energies are spatially correlated, with the correlation function decaying as a power-law of the molecular separation.¹⁰⁵

In conjugated polymers, however, structural defects along the chain (e.g., chemical defects or backbone twists) can break the conjugation between two successive monomers. As a result, charge does not delocalize over the entire chain and chains are partitioned on conjugated segments of different lengths. This broadens the distribution of ionization potentials for holes (electron affinities for electrons), contributing to the overall DOS broadening. Since this broadening is intimately linked to the micro- and mesoscale morphology of a partially ordered mesophase, it is not only difficult to extract the broadening from experimental data, but also from computer simulations (notably due to the extremely slow dynamics of long chains).

Evaluation of the external contribution to the site energetics, which accounts for electrostatic and induction interactions between segments, requires substituting the atomistic detail back into the soft-sphere morphologies. To a first approximation, however, one can neglect this intermolecular contribution to the DOS due to the absence of large partial charges or dipoles in P3HT, such that the variation of energy levels due to a change in conjugation length dominates the width of the density of states. With the soft-model-based mesoscale morphologies at hand we can calculate this internal contribution to the DOS, study spatial correlations of site energies, and evaluate the temperature dependence (note that

in small-molecule-based organic semiconductors the “internal” DOS is temperature-independent).

For this purpose, we choose $\bar{\nu} = \bar{\mu} = 0$ and $\bar{\lambda} = 5.5k_B T_0$; i.e., we select a set of parameters well inside the biaxial phase (see Figure 5a) for all the considered chain lengths. In a limited number of cases, for the two longest chains $N = 16$ and $N = 32$, a weaker coupling strength $\bar{\lambda} = 5k_B T_0$ has been also considered to increase sensitivity to temperature changes. A representative snapshot of an equilibrated system used for calculating properties related to charge-transport is shown in Figure 4b.

A. Distribution of Conjugation Lengths. We first evaluate the distributions of conjugation lengths in the isotropic and biaxial nematic phases as a function of length and temperature. To partition a chain into conjugated segments we employ a heuristic criterion based on the dihedral angle between two successive monomers: If this angle deviates from the planar *cis* and *trans* conformations by more than $\pm 45^\circ$, the conjugation is assumed to be broken across the monomer–monomer bond.¹⁰⁶ The conjugation length is then the number of monomers l that are part of this conjugated segment. By analyzing in this fashion a large number of Monte Carlo snapshots of systems with different ordering and molecular weights, we obtain the number density $\rho_s(l, N)$, that is, the number of conjugated segments of length l per unit volume. These number densities are shown in Figure 7a for both isotropic and biaxial melts.

The functional dependence of ρ_s on l for different molecular weights can be understood with a simple analytical estimation. Let us introduce a probability p of preserving the conjugation across a monomer–monomer bond, so that $p = 0$ implies N conjugated segments in each chain, while $p = 1$ corresponds to one conjugated segment of length N (i.e., the entire chain is conjugated). The probability to find a conjugated segment of length l inside a chain of length N is proportional to the probability of finding $l - 1$ conjugated bonds, p^{l-1} , and two broken conjugations, $(1 - p)^2$, weighted by the number of possible placements of a segment of length l along a chain of length N , $(N - l + 1)$. Similarly, the probability of finding a conjugated segment of length l at the chain ends is proportional to $2(1 - p)p^{l-1}$. Hence, the number density of segments of length l , $\rho_s(l, N)$, reads

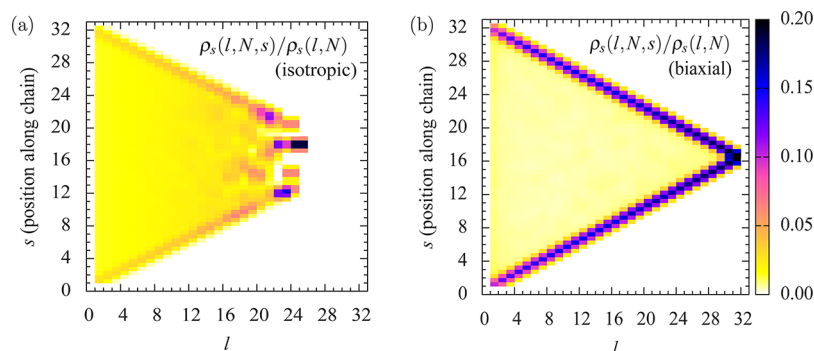


Figure 8. (a) Partial density $\rho_s(l, N, s)$ of segments with conjugation length l at position s in the chain, normalized by the segment density $\rho_s(l, N)$ for the (a) isotropic and (b) biaxial morphologies. The plots highlight how conjugation defects tend to localize near the terminal monomers in the case of biaxial nematic order, as opposed to a homogeneous along-the-chain defect distribution for isotropic systems. The data were obtained for $N = 32$ at $\bar{\lambda} = 5.5k_B T_0$ and $T = T_0 = 500$ K.

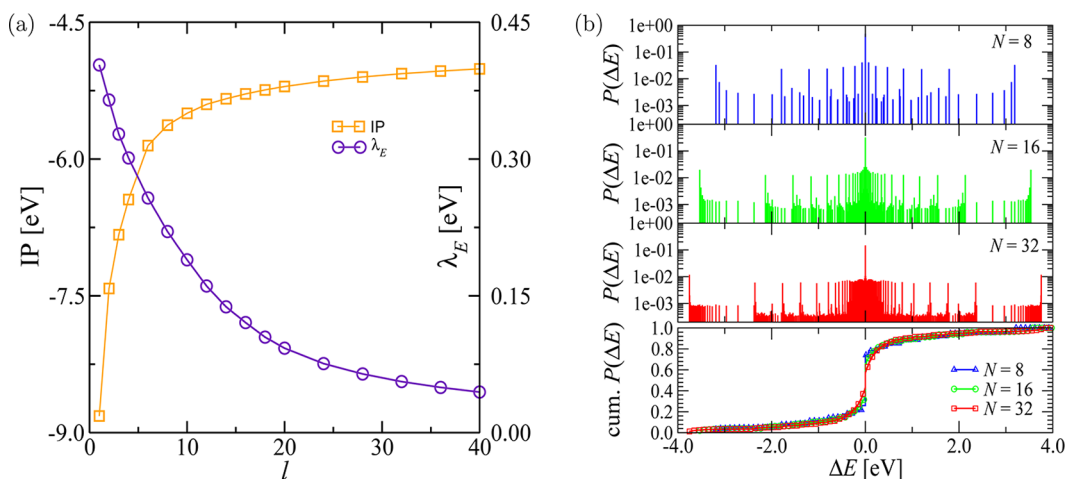


Figure 9. (a) Gas-phase ionization potentials and charge-transfer reorganization energies calculated for different conjugation lengths l . All calculations were performed using density functional theory with the B3LYP functional and the 6-311g basis set. Reorganization energies were estimated assuming harmonic potentials for charged and neutral states. For calculation details see ref 108. (b) Top three panels: discrete pair-energy distributions for biaxial systems with chain lengths $N = 8$, $N = 16$, and $N = 32$, calculated from a particle-based neighbor-list with cutoff 1.0 nm. Bottom panel: cumulative pair-energy distribution. Increasing molecular weight leads to a stronger fragmentation of energy levels, yet the shape of the cumulative distribution is unaffected by the chain-length increase. The data were obtained for $\bar{\lambda} = 5.5k_B T_0$ and $T = T_0 = 500$ K.

$$\frac{\rho_s(l, N)}{\rho_0} \approx \left[\left(1 - \frac{l+1}{N} \right) (1-p)^2 + \frac{2}{N} (1-p) \right] p^{l-1} \quad (14)$$

where ρ_0 is the average number density of the thiophene monomers in the system. The derivation of eq 14 ignores intrachain torsional correlations, since we discern between “internal” and “tail” segments but neglect the constraint that the lengths of all conjugated segments in a chain should add up to N . The latter can be taken into account,¹⁰⁷ but for a qualitative description eq 14 suffices.

Considering the conjugation criterion of $\pm 45^\circ$ and assuming that in the isotropic mesophase all torsional degrees of freedom are independently and canonically sampled we can estimate p as $p = 1 - 2Z^{-1} \int_{\pi/4}^{3\pi/4} \exp(-V_\phi/kT) d\phi$, with $Z = \int_0^{2\pi} \exp(-V_\phi/kT) d\phi$. The resulting $p = 0.58$ gives rise to a substantial population of short “internal” segments and end-effects become insignificant; i.e., the limit of the infinitely long chain is applicable. In this case ($l \ll N$, $(1-p) \gg 2/N$) eq 14 yields $\rho_s/\rho_0 \sim (1-p)^2 p^{l-1}$, i.e., $\ln \rho_s$ scales as $l - 1$ and is independent of N as observed in Figure 7a. Note that the probability $p = 0.56$

extracted from the fit in Figure 7a is very close to the initial estimate.

In a biaxial nematic, polymer backbones are planar and $p \sim 1$. The conjugated segments are long and, for relatively short polymers, end effects lead to a chain-length dependent ρ_s , as shown in Figure 7a. Equation 14 in the limit of $(1-p) \ll 2/N$ predicts $\rho_s/\rho_0 \sim (1/N)(1-p)p^{l-1}$. That the condition $(1-p) \ll 2/N$ holds in our case can be verified by plotting the ratio $Nl\rho_s/\rho_0$ versus l . Indeed, the inset of Figure 7a shows how all distributions then collapse on a single master curve. For longer chains, however, it might happen that $2/N \ll (1-p)$ and ρ_s will be dominated by contributions from “internal” conjugated segments, as in the isotropic mesophase. For example, at 400 K, where $p = 0.98$ (see the inset of Figure 7b), this would correspond to $N \gg 100$, well beyond the chain lengths studied here.

The bond conjugation probability p can, to some extent, serve as an order parameter for chain conjugation: As shown in Figure 7b, starting at low temperatures and strong biaxial order, p decreases upon increasing temperature. The T -dependence of p is shown in the inset of Figure 7b, together with a fit to a

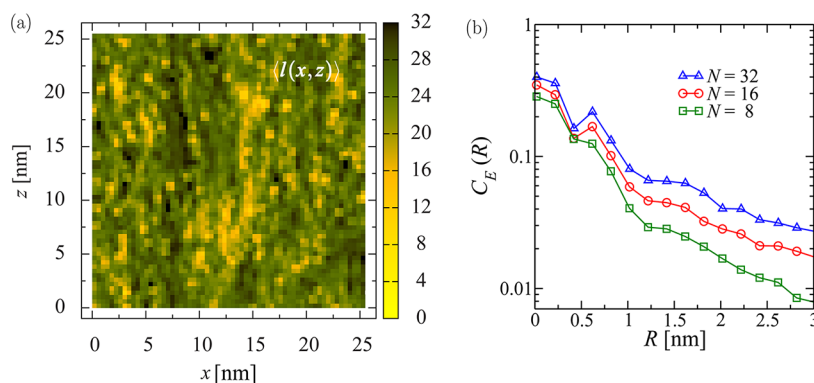


Figure 10. (a) Contour plot of the local average conjugation length, $\langle l(x, z) \rangle$, where averaging occurs over a 5 nm slice in the y -direction and 0.16 nm^2 bins in the x - z plane. The thiophenes have their $\mathbf{n}_i^{(1)}(s)$, $\mathbf{n}_i^{(2)}(s)$, and $\mathbf{n}_i^{(3)}(s)$ vectors aligned (on average) along the z , x , and y -directions, respectively (cf., Figure 4b). (b) Spatial internal site-energy correlation function for biaxial ordering. The data were obtained at $\bar{\lambda} = 5.5k_B T_0$ and $T = T_0 = 500 \text{ K}$.

power-law dependence $p(T) = p_0 + a(1 - T/T')^b$ with $b \simeq 0.06$, $a \simeq 0.5$, and $T' = 540 \text{ K}$.

B. Position of a Segment in a Chain. As discussed above for the biaxial mesophases, the distribution of conjugation lengths (for $l \neq N$) is well described by a model accounting only for the segments at the chain ends. One can therefore conclude that for the lengths of chains considered here, there will be an increased concentration of torsional defects toward the *terminal monomers*. The situation is very different in isotropic melts, where, due to the large number of "internal" conjugated segments, the defects are distributed more homogeneously along the backbone. This is illustrated in Figure 8a and Figure 8b, where the density ratio $\rho_s(l, N, s)/\rho_s(l, N)$, i.e., the probability for the center of a conjugated segment of length l to be at a position s along the chain, is shown for isotropic and biaxial morphologies, respectively. For short polymers the reason for defects to concentrate toward the chain ends in the case of biaxial order is intuitively clear: First, creating an isolated (in terms of conjugation) monomer in the middle of a conjugated-polymer chain requires two torsional defects instead of just one for terminating thiophenes (cf., eq 14). Second, for polythiophenes, a change in dihedral angle entails a change in chain direction due to the special geometry of the thiophene–thiophene connection; this direction change is thwarted by nonbonded interactions with neighboring chains.

How do the above results relate to the description of charge transport? It is noteworthy that short conjugated segments can act as kinetic traps during charge transport in spite of their higher site energy: Because of the large difference in site energy between segments i and j , $\Delta E = E_i - E_j$, charge hopping may occur in the inverted regime, where the sum of the reorganization energies λ_E , shown in Figure 9a, is smaller than ΔE , thus promoting slow rates for charge transfer. Investigating this quantitatively requires taking into account the electrostatic and polarization effects on the energy levels, since a stronger localization of the hole leads to an enhanced stabilization due to induction, reducing ΔE compared to the gas-phase calculation.

C. Density of States. The density of conjugated segments can be translated into the energetic density of states for holes according to the aforementioned relation between the conjugation length l and the gas-phase ionization potential (IP, Figure 9a). In order to more closely reflect transport conditions, we do not consider the single-site DOS, but a two-site DOS $P(\Delta E)$ based on pairs of segments. These pairs are

drawn from a monomer-based neighbor-list with cutoff $R_c = 1.0 \text{ nm}$. The energy ΔE that enters into the two-site DOS is the site-energy difference between the two participating segments. The associated probability density $P(\Delta E)$ is by definition symmetric about $\Delta E = 0$, see Figure 9b. The advantages of the two-site DOS are 2-fold: First, it not only takes into account the conventional single-site DOS, but also correlations of the energy landscape (see the next subsection and refs 108–110). Second, charge transfer rates within Marcus theory only depend on site-energy differences ΔE , thus making $P(\Delta E)$ the preferred measure to assess transport conditions.

Before discussing molecular weight, we will elaborate on the spectrum structure. Note that we only consider the internal contribution to the site energies, hence the pair-energy distribution features delta-peaks at characteristic energy level separations. For all molecular weights, the spike at $\Delta E = 0$ with $P > 0.1$ is by far the most pronounced (note the semi-logarithmic scale in Figure 9b), as is a result of the strong biaxial nematic order in these systems, with a large fraction of the chains in their fully conjugated configuration.

Next, there is a number of peaks of intensity $P \sim 0.01$ distributed over a very wide energy range $0 \text{ eV} < |\Delta E| < 4 \text{ eV}$: These are hopping pairs formed between a fully conjugated chain ($l = N$) and a conjugated subunit ($l < N$). It is striking that the peaks that can be allocated to pairs of this nature are all located around the same density level, $P \sim 0.01$. Hence, located on a fully conjugated chain, a hole encounters mostly neighboring segments with $l = N$, and then, with a reduced but constant probability, a set of partially conjugated hopping destinations with delocalization length l anywhere from 1 to $N - 1$. This can be related back to the density of segments $\rho_s(l, N)$, which exhibits a broad plateau when reweighted according to volume, as in $l\rho_s(l, N)$.

Finally, a third type of pairs, with a probability density of $P \sim 0.001$ and pair energies again spread over the whole spectrum, is associated with neighbors formed between two conjugated subunits of length $l < N$. These pairs are, however, sparse, and we can expect their effect on transport to be small.

The role of pairs with nonzero ΔE at $P \sim 0.01$ is not obvious, and there are two scenarios to be considered. For the first one, we refer back to our discussion of the inverted regime, where ΔE exceeds the reorganization energy: This case affects pairs located toward the periphery of the spectrum, potentially resulting in inverted traps. Second, we picture a fully conjugated chain sandwiched in between two conjugated subunits in a 1D-

connected network, where the nonzero pair-energies would be sampled from the spectrum center, creating a mild energetic trap. At this point, we would like to note again that induction stabilizes segments with large l weaker than segments with small l . Polarization therefore leads to a compression of the spectrum that is not taken into account here, but that will enable short segments to more easily participate in charge transport, making the above two scenarios even more relevant.

We now turn to the molecular-weight dependence: Increasing the chain length from $N = 8$ to $N = 32$, more and more energy levels are introduced to the system. Yet, the cumulative two-site DOS, $\int_{-\infty}^{\Delta E} P(E) dE$ illustrates that the overall distribution remains almost unchanged: The largest differences occur toward the center ($\Delta E = 0$) of the distribution (where the introduction of more energy levels for higher molecular weights broadens the DOS), and at the periphery (where the distribution extends to larger $|\Delta E|$ due to longer available conjugation lengths). These are however mild effects that can be compensated by the broadening of around 0.1 eV expected to result from electrostatic effects, as well as the overall narrowing of the spectrum due to polarization. We conclude that within the range of molecular weights studied here, the dependence of transport on chain length is indeed small, as previously suggested by experiment.⁹⁴

D. Spatial Correlations. In small-molecule-based amorphous organic semiconductors site energies are spatially correlated. The origin of these correlations is the long-range nature of electrostatic interactions, for instance due to the presence of molecular dipoles. The internal contribution to the DOS (due to changes in molecular conformations) is not spatially correlated for amorphous semiconductors. We, however, should not expect this for polymeric semiconductors. Here, the distribution of conjugated segments can be spatially correlated due to long-range orientational ordering, as shown in Figure 10a. Moreover, it can also be anticorrelated, since a single chain might not be able to accommodate several long conjugated segments.

In order to quantify these effects we calculate the spatial correlation function $C_E(R)$ of internal site energies,

$$C_E(R) = \frac{\langle (E_i - \langle E \rangle)(E_j - \langle E \rangle) \rangle_{r_{ij}=R}}{\sigma_E^2} \quad (15)$$

where $\langle E \rangle$ is the average and σ_E^2 is the variance of the site-energy distribution, and averaging occurs over all pairs (i, j) of conjugated segments of smallest distance of approach r_{ij} with $R \leq r_{ij} \leq R + dR$. This correlation function is shown for biaxial phases in Figure 10b. Note that the dip at 0.4 nm, corresponding to the bond length between successive monomers of the same chain, points to a negative intrachain correlation of site energies, as is expected due to the finite length of the chain. Interestingly, despite only taking into account the internal contribution to the site energies, the energetic landscape is weakly and positively correlated over a range of 1.2 nm, with a tail as far down as 3 nm. The correlation becomes more pronounced as N increases and can be traced back to the coexistence of ordered and disordered regions in the morphology as illustrated by Figure 10a. Reinserting atomistic details into the morphology should not affect this supramolecular arrangement and we expect that the qualitative features of the correlation function will persist. This reinsertion will however be necessary to quantitatively assess the effect of

the difference in site-energy correlation, seen for the three molecular weights, on mobility.

On a final note, a correlated energy landscape usually results from the surrounding electrostatic environment, for instance due to the presence of molecular dipoles. Our results suggest that in polymeric mesophases, an additional correlation arises from accumulating torsional defects, which perturb the local environment, next to the presence of strongly ordered biaxial domains. It can be expected, that this perturbation is particularly pronounced in polythiophenes, again due to the change in chain direction that is associated with the torsional movement.

VI. CONCLUSIONS AND OUTLOOK

To summarize, we have developed a coarse-grained model capable of generating liquid crystalline ordering and mesoscale-size morphologies of polymeric semiconductors. The model combines bonded interactions parametrized on the distributions obtained via sampling of an atomistic chain, in this case poly(3-hexylthiophene) (P3HT), with nonbonded interactions represented by soft anisotropic potentials. We demonstrate that this model is capable of describing uniaxial and biaxial nematic ordering in a P3HT melt. Similar long-range (nematic and smectic) ordering has been observed experimentally in various poly(3-alkylthiophenes).^{32,33,35,38,41}

Using the developed model, we have calculated thermodynamic and elastic properties of liquid crystalline phases and found that weaker anisotropic interactions are required to induce nematic ordering in a system with longer chains, in agreement with experimental observations.³⁸ Despite the softness of the nonbonded interactions, the calculated Frank elastic constants are shown to have values typical for polymeric liquid crystals,^{92,93} with the bend and twist constants on the order of 10^{-11} N and a significantly larger splay constant.

With the mesoscale morphologies at hand, we have analyzed the conjugated-segment-length distributions. In isotropic melts, the distribution of dihedral angles is canonical and conjugation-breaking defects are uniformly distributed along the chain. In nematic phases, both distributions are affected by long-range correlations between chain orientations and (for the relatively short polymers considered here) defects tend to localize near chain ends. This has an important implication for the broadening of the density of states, which is due to the difference in ionization potentials between conjugated segments of different lengths. We show that the distribution of site energies is non-Gaussian, and that site energies are spatially correlated due to correlated alignment of neighboring chains. There is, however, a certain degree of anticorrelation at short distances due to several conjugated segments sharing the same chain. We point out that, in spite of their relatively high energies, short conjugated segments can act as kinetic traps during charge transport, provided that charge hopping occurs in the Marcus inverted region.

As an outlook, we mention that it is important to extend the model to nonbonded interactions allowing for spatially structured molecular arrangements, such as smectic^{35,41} and lamellar mesophases.

■ ASSOCIATED CONTENT

Supporting Information

Pairwise directional interactions and functionals of collective variables. This material is available free of charge via the Internet at <http://pubs.acs.org>.

■ AUTHOR INFORMATION

Corresponding Author

*E-mail: (K.C.D.) daoulas@mpip-mainz.mpg.de.

Notes

The authors declare no competing financial interest.

■ ACKNOWLEDGMENTS

We are grateful to Mara Jochum and Karen Johnston for critical reading of the manuscript. We have benefited from stimulating discussions with Frédéric Laquai, Hsiao-Ping Hsu, Marcus Müller, Natalie Stingelin, and Thomas Thurn-Albrecht. This work was partially supported by the DFG Program IRTG 1404, DFG Grant SPP 1355, and BMBF Grants MORPHEUS (FKZ 13N11704), MEDOS (FKZ 03EK3503B), and MESOMERIE (FKZ 13N10723).

■ REFERENCES

- (1) McCullough, R. D. *Adv. Mater.* **1998**, *10*, 93–116.
- (2) McCulloch, I.; Heeney, M.; Chabinyc, M. L.; DeLongchamp, D.; Kline, R. J.; Coelle, M.; Duffy, W.; Fischer, D.; Gundlach, D.; Hamadani, B.; Hamilton, R.; Richter, L.; Salleo, A.; Shkunov, M.; Sporrowe, D.; Tierney, S.; Zhong, W. *Adv. Mater.* **2009**, *21*, 1091–1109.
- (3) Boudreault, P. L. T.; Najari, A.; Leclerc, M. *Chem. Mater.* **2010**, *23*, 456–469.
- (4) McCulloch, I.; Ashraf, R. S.; Biniek, L.; Bronstein, H.; Combe, C.; Donaghey, J. E.; James, D. I.; Nielsen, C. B.; Schroeder, B. C.; Zhang, W. *Acc. Chem. Res.* **2012**, *45*, 714–722.
- (5) Polyera achieves 5.2% all-polymer organic solar cells - polyera corporation. <http://www.polyera.com/newsflash/polyera-achieves-5-2-all-polymer-organic-solar-cells>, 2012.
- (6) Roncali, J. *Chem. Rev.* **1997**, *97*, 173–206.
- (7) Peet, J.; Kim, J. Y.; Coates, N. E.; Ma, W. L.; Moses, D.; Heeger, A. J.; Bazan, G. C. *Nat. Mater.* **2007**, *6*, 497–500.
- (8) Agostinelli, T.; Ferenczi, T. A. M.; Pires, E.; Foster, S.; Maurano, A.; Müller, C.; Ballantyne, A.; Hampton, M.; Lilliu, S.; Campoy-Quiles, M.; Azimi, H.; Morana, M.; Bradley, D. D. C.; Durrant, J.; MacDonald, J. E.; Stingelin, N.; Nelson, J. J. *Polym. Sci., Polym. Phys.* **2011**, *49*, 717–724.
- (9) That is, form different crystal structures depending on processing conditions.
- (10) Prosa, T. J.; Winokur, M. J.; McCullough, R. D. *Macromolecules* **1996**, *29*, 3654–3656.
- (11) Yuan, Y.; Zhang, J.; Sun, J.; Hu, J.; Zhang, T.; Duan, Y. *Macromolecules* **2011**, *44*, 9341–9350.
- (12) Marcon, V.; Breiby, D. W.; Pisula, W.; Dahl, J.; Kirkpatrick, J.; Patwardhan, S.; Grozema, F.; Andrienko, D. *J. Am. Chem. Soc.* **2009**, *131*, 11426–11432.
- (13) Pascui, O. F.; Lohwasser, R.; Sommer, M.; Thelakkat, M.; Thurn-Albrecht, T.; Saalwachter, K. *Macromolecules* **2010**, *43*, 9401–9410.
- (14) Lu, X.; Hlaing, H.; Germack, D. S.; Peet, J.; Jo, W. H.; Andrienko, D.; Kremer, K.; Ocko, B. M. *Nat. Commun.* **2012**, *3*, 795.
- (15) Dudenko, D.; Kiersnowski, A.; Shu, J.; Pisula, W.; Sebastiani, D.; Spiess, H. W.; Hansen, M. R. *Angew. Chem., Int. Ed.* **2012**, *124*, 11230–11234.
- (16) Louis, A. A.; Bolhuis, P. G.; Hansen, J. P. *Phys. Rev. E* **2000**, *62*, 7961–7972.
- (17) Likos, C. *Soft Matter* **2006**, *2*, 478–498.
- (18) Klapp, S. H. L.; Diestler, D. J.; Schoen, M. *J. Phys.-Condens. Matter* **2004**, *16*, 7331–7352.
- (19) Warren, P. B. *Curr. Opin. Colloid Interface* **1998**, *3*, 620–624.
- (20) Lang, A.; Likos, C.; Watzlawek, M.; Löwen, H. *J. Phys.-Condens. Mat.* **2000**, *12*, 5087–5108.
- (21) Laradji, M.; Guo, H.; Zuckermann, M. J. *Phys. Rev. E* **1994**, *49*, 3199–3206.
- (22) Pagonabarraga, I.; Frenkel, D. *J. Chem. Phys.* **2001**, *115*, 5015–5026.
- (23) Fredrickson, G.; Ganesan, V.; Drolet, F. *Macromolecules* **2002**, *35*, 16–39.
- (24) Ganesan, V.; Pryamitsyn, V. *J. Chem. Phys.* **2003**, *118*, 4345–4348.
- (25) Düchs, D.; Schmid, F. *J. Chem. Phys.* **2004**, *121*, 2798–2805.
- (26) Daoulas, K. C.; Müller, M. *J. Chem. Phys.* **2006**, *125*, 184904.
- (27) Daoulas, K. C.; Rühle, V.; Kremer, K. *J. Phys.-Condens. Mat.* **2012**, *24*, 284121.
- (28) Pike, D. Q.; Datchevy, F. A.; Müller, M.; de Pablo, J. J. *J. Chem. Phys.* **2009**, *131*, 084903.
- (29) Wang, Q.; Yin, Y. *J. Chem. Phys.* **2009**, *130*, 104903.
- (30) Müller, M. *J. Stat. Phys.* **2011**, *145*, 967–1016.
- (31) Straley, J. *Phys. Rev. A* **1974**, *10*, 1881–1887.
- (32) Winokur, M.; Spiegel, D.; Kim, Y.; Hotta, S.; Heeger, A. *Synth. Met.* **1989**, *28*, 419–426.
- (33) Zhao, Y.; Yuan, G.; Roche, P.; Leclerc, M. *Polymer* **1995**, *36*, 2211–2214.
- (34) DeLongchamp, D.; Kline, R.; Jung, Y.; Lin, E.; Fischer, D.; Gundlach, D.; Cotts, S.; Moad, A.; Richter, L.; Toney, M.; Heeney, M.; McCulloch, I. *Macromolecules* **2008**, *41*, 5709–5715.
- (35) Hugger, S.; Thomann, R.; Heinzl, T.; Thurn-Albrecht, T. *Colloid Polym. Sci.* **2004**, *282*, 932–938.
- (36) Chabinyc, M. *J. Vac. Sci. Technol. B* **2008**, *26*, 445–457.
- (37) McCulloch, I.; Heeney, M.; Bailey, C.; Genevicius, K.; MacDonald, I.; Shkunov, M.; Sparrowe, D.; Tierney, S.; Wagner, R.; Zhang, W.; Chabinyc, M.; Kline, R.; McGehee, M.; Toney, M. *Nat. Mater.* **2006**, *5*, 328–333.
- (38) Ho, V.; Boudouris, B.; Segalman, R. *Macromolecules* **2010**, *43*, 7895–7899.
- (39) Grell, M.; Bradley, D. *Adv. Mater.* **1999**, *11*, 895–905.
- (40) Stingelin, N. *Polym. Int.* **2012**, *61*, 866–873.
- (41) Wu, Z.; Petzold, A.; Henze, T.; Thurn-Albrecht, T.; Lohwasser, L. H.; Sommer, M.; Thelakkat, M. *Macromolecules* **2010**, *43*, 4646–4653.
- (42) Kremer, K.; Müller-Plathe, F. *Mol. Simul.* **2002**, *28*, 729–750.
- (43) Fritz, D.; Harmandaris, V.; Kremer, K.; van der Vegt, N. *Macromolecules* **2009**, *42*, 7579–7588.
- (44) Hess, B.; Kutzner, C.; van der Spoel, D.; Lindahl, E. *J. Chem. Theory Comput.* **2008**, *4*, 435–447.
- (45) Jorgensen, W. L.; Tirado-Rives, J. *J. Am. Chem. Soc.* **1988**, *110*, 1657–1666.
- (46) McDonald, N. A.; Jorgensen, W. L. *J. Phys. Chem. B* **1998**, *102*, 8049–8059.
- (47) DuBay, K. H.; Hall, M. L.; Hughes, T. F.; Wu, C.; Reichman, D. R.; Friesner, R. A. *J. Chem. Theory Comput.* **2012**, *8*, 4556–4569.
- (48) Poelking, C.; Andrienko, D. *Adv. Polym. Sci.* **2013**.
- (49) Rühle, V.; Junghans, C.; Lukyanov, A.; Kremer, K.; Andrienko, D. *J. Chem. Theory Comput.* **2009**, *9*, 3211–3223.
- (50) Jochum, M.; Andrienko, D.; Kremer, K.; Peter, C. *J. Chem. Phys.* **2012**, *137*, 064102.
- (51) Mukherjee, B.; Delle Site, L.; Kremer, K.; Peter, C. *J. Phys. Chem. B* **2012**, *116*, 8474–8484.
- (52) Sonnet, A. M.; Virga, E. G.; Durand, G. E. *Phys. Rev. E* **2003**, *67*, 061701.
- (53) Matteis, G.; Sonnet, A. M.; Virga, E. *Continuum Mech. Therm.* **2008**, *20*, 347–374.
- (54) Sonnet, A. M.; Virga, E. G. *Phys. Rev. E* **2008**, *77*, 031704.
- (55) Bird, R. B.; Stewart, W.; Lightfoot, E. *Transport phenomena*; Wiley: New York, 1960.
- (56) Luckhurst, G.; Zannoni, C.; Nordio, P.; Segre, U. *Mol. Phys.* **1975**, *30*, 1345–1358.
- (57) Steele, W. J. *J. Chem. Phys.* **1963**, *39*, 3197–3208.
- (58) Berardi, R.; Fava, C.; Zannoni, C. *Chem. Phys. Lett.* **1995**, *236*, 462–468.
- (59) Vink, R. L. C.; Schilling, T. *Phys. Rev. E* **2005**, *71*, 051716.
- (60) Prestipino, S.; Saija, F. *J. Chem. Phys.* **2007**, *126*, 194902.

- (61) Hughes, Z.; Stimson, L.; Slim, H.; Lintuvuori, J.; Ilnytskyi, J.; Wilson, M. *Comput. Phys. Commun.* **2008**, *178*, 724–731.
- (62) Wilson, M. R. *Int. Rev. Phys. Chem.* **2005**, *24*, 421–455.
- (63) Zong, J.; Zhang, X.; Wang, Q. *J. Chem. Phys.* **2012**, *137*, 134904.
- (64) Chou, S.-H.; Tsao, H.-K.; Sheng, Y.-J. *J. Chem. Phys.* **2011**, *134*, 034904.
- (65) Lintuvuori, J.; Wilson, M. *J. Chem. Phys.* **2008**, *128*, 044906.
- (66) Hamm, M.; Goldbeck-Wood, G.; Zvelindovsky, A. V.; Sevink, G. J. A.; Fraaije, J. G. E. M. *J. Chem. Phys.* **2002**, *116*, 3152–3161.
- (67) Pryamitsyn, V.; Ganesan, V. *J. Chem. Phys.* **2004**, *120*, 5824–5838.
- (68) Wang, Q. *Soft Matter* **2011**, *7*, 3711–3716.
- (69) Kriksin, Y.; Khalatur, P. *Macromol. Theor. Simul.* **2012**, *21*, 382–399.
- (70) Kozub, D. R.; Vakhshouri, K.; Orme, L. M.; Wang, C.; Hexemer, A.; D, G. E. *Macromolecules* **2011**, *44*, 5722–5726.
- (71) Kron, A. *Polym. Sci. USSR* **1965**, *7*, 1361–1367.
- (72) Wall, F.; Mandel, F. *J. Chem. Phys.* **1975**, *63*, 4592–4595.
- (73) Vacatello, M.; Avitabile, G.; Corradini, P.; Tuzi, A. *J. Chem. Phys.* **1980**, *63*, 548–552.
- (74) Dodd, L. R.; Boone, T. D.; Theodorou, D. N. *Mol. Phys.* **1993**, *78*, 961–996.
- (75) Holtzer, A. *J. Polym. Sci.* **1955**, *17*, 432–434.
- (76) Cesar, B.; Rawiso, M.; Mathis, A.; François, B. *Synth. Met.* **1997**, *84*, 241–242.
- (77) Hsu, H.-P.; Paul, W.; Binder, K. *Macromolecules* **2010**, *43*, 3094–3102.
- (78) McCulloch, B.; Ho, V.; Hoarfrost, M.; Stanley, C.; Do, C.; Heller, W. T.; Segalman, R. A. *Macromolecules* **2013**, *46*, 1899–1907.
- (79) Sharp, P.; Bloomfield, V. *Biopolymers* **1968**, *6*, 1201–1211.
- (80) Pötschke, D.; Hickl, P.; Ballauff, M.; Åstrand, P.-O.; Pedersen, J. S. *Macromol. Theor. Simul.* **2000**, *9*, 345–353.
- (81) Hansen, J. P.; McDonald, I. I. R. *Theory of Simple Liquids*. Academic Press: San Diego, CA, 2006.
- (82) Huang, D. M.; Faller, R.; Do, K.; Moul, A. J. *J. Chem. Theory Comput.* **2010**, *6*, 526–537.
- (83) Allen, M. P. *Liq. Cryst.* **1990**, *8*, 499–511.
- (84) Low, R. *Eur. J. Phys.* **2002**, *23*, 111–117.
- (85) Eppenga, R.; Frenkel, D. *Mol. Phys.* **1984**, *52*, 1303–1334.
- (86) Kléman, M.; Lavrentovich, O. *Soft Matter Physics: An Introduction*. Springer: 2002.
- (87) Allen, M.; Warren, M.; Wilson, M.; Sauron, A.; Smith, W. J. *J. Chem. Phys.* **1996**, *105*, 2850–2858.
- (88) Phuong, N. H.; Germano, G.; Schmid, F. *J. Chem. Phys.* **2001**, *115*, 7227–7234.
- (89) De Gennes, P. G. *Mol. Cryst. Liq. Cryst.* **1976**, *34*, 177–182.
- (90) Lee, S.; Meyer, R. B. *Liq. Cryst.* **1990**, *7*, 15–29.
- (91) Z.-M, S.; Kléman, M. *Mol. Cryst. Liq. Cryst.* **1984**, *111*, 321–328.
- (92) Kléman, M. *Faraday Discuss. Chem. Soc.* **1985**, *79*, 215–224.
- (93) Frezzato, D.; Moro, G. J.; Tittelbach, M.; Kothe, G. *J. Chem. Phys.* **2003**, *119*, 4060–4069.
- (94) Ballantyne, A. M.; Chen, L.; Dane, J.; Hammant, T.; Braun, F. M.; Heeney, M.; Duffy, W.; McCulloch, I.; Bradley, D. D. C.; Nelson, J. *Adv. Funct. Mater.* **2008**, *18*, 2373–2380.
- (95) Kline, R. J.; McGehee, M. D.; Kadnikova, E. N.; Liu, J.; Frchet, J. M. J.; Toney, M. F. *Macromolecules* **2005**, *38*, 3312–3319.
- (96) Zen, A.; Pflaum, J.; Hirschmann, S.; Zhuang, W.; Jaiser, F.; Asawapirom, U.; Rabe, J. P.; Scherf, U.; Neher, D. *Adv. Funct. Mater.* **2004**, *14*, 757–764.
- (97) Moreno, M.; Casalegno, M.; Raos, G.; Meille, S. V.; Po, R. *J. Phys. Chem. B* **2010**, *114*, 1591–1602.
- (98) Do, K.; Huang, D. M.; Faller, R.; Moul, A. J. *J. Phys. Chem. Chem. Phys.* **2010**, *12*, 14735–14739.
- (99) McMahon, D. P.; Cheung, D. L.; Goris, L.; Dacuna, J.; Salleo, A.; Troisi, A. *J. Phys. Chem. C* **2011**, *115*, 19386–19393.
- (100) Kwiatkowski, J. J.; Jimison, L. H.; Salleo, A.; Spakowitz, A. J. *J. Appl. Phys.* **2011**, *109*, 113720.
- (101) Bouhassoune, M.; Mensfoort, S. v.; Bobbert, P.; Coehoorn, R. *Org. Electron.* **2009**, *10*, 437–445.
- (102) Coehoorn, R.; Pasveer, W. F.; Bobbert, P. A.; Michels, M. A. J. *Phys. Rev. B* **2005**, *72*, 155206.
- (103) Baessler, H. *Phys. Status Solidi B* **1993**, *175*, 15–56.
- (104) May, F.; Baumeier, B.; Lennartz, C.; Andrienko, D. *Phys. Rev. Lett.* **2012**, *109*, 136401.
- (105) Novikov, S. V.; Vannikov, A. V. *J. Phys. Chem. C* **2009**, *113*, 2532–2540.
- (106) Rühle, V.; Kirkpatrick, J.; Andrienko, D. *J. Chem. Phys.* **2010**, *132*, 134103.
- (107) Kohler, B.; Woehl, J. *J. Chem. Phys.* **1995**, *103*, 6253.
- (108) Rühle, V.; Lukyanov, A.; May, F.; Schrader, M.; Vehoff, T.; Kirkpatrick, J.; Baumeier, B.; Andrienko, D. *J. Chem. Theory Comput.* **2011**, *7*, 3335–3345.
- (109) Schrader, M.; Körner, C.; Elschner, C.; Andrienko, D. *J. Mater. Chem.* **2012**, *22*, 22258.
- (110) Schrader, M.; Fitzner, R.; Hein, M.; Elschner, C.; Baumeier, B.; Leo, K.; Riede, M.; Bäuerle, P.; Andrienko, D. *J. Am. Chem. Soc.* **2012**, *134*, 6052–6056.